

Modeling a semiconductor laser with an intracavity atomic absorberC. Masoller,^{1,*} M. Oria,^{2,†} and R. Vilaseca^{1,‡}¹*Departament de Física i Enginyeria Nuclear, Universitat Politècnica de Catalunya, Colom 11, Terrassa 08222, Barcelona, Spain*²*Laboratório de Física Atômica e Lasers, Universidade Federal da Paraíba, 58051-970 João Pessoa–PB, Brazil*

(Received 24 July 2008; published 28 July 2009)

The dynamics of a semiconductor laser with an intracavity atomic absorber is studied numerically. The study is motivated by the experiments of Barbosa *et al.* [Opt. Lett. **32**, 1869 (2007)], using a semiconductor junction as an active medium, with its output face being antireflection coated, and a cell containing cesium vapor placed in a cavity that was closed by a diffraction grating (DG). The DG allowed scanning the lasing frequency across the D_2 line in the Cs spectrum, and different regimes such as frequency bistability or dynamic instability were observed depending on the operating conditions. Here we propose a rate-equation model that takes into account the dispersive losses and the dispersive refractive index change in the laser cavity caused by the presence of the Cs vapor cell. These effects are described through a modification of the complex susceptibility. The numerical results are found to be in qualitative good agreement with some of the observations; however, some discrepancies are also noticed, which can be attributed to multi-longitudinal-mode emission in the experiments. The simulations clearly show the relevant role of the Lamb dips and crossover resonances, which arise on top of the Doppler-broadened D_2 line in the Cs spectrum, and are due to the forward and backward intracavity fields interacting resonantly with the Cs atoms. When the laser frequency is locked in a dip, a reduction in the frequency noise and of the intensity noise is demonstrated.

DOI: [10.1103/PhysRevA.80.013830](https://doi.org/10.1103/PhysRevA.80.013830)

PACS number(s): 42.55.Px, 42.60.Mi, 42.62.Fi, 42.50.Ct

I. INTRODUCTION

Nonlinear laser absorption spectroscopy is receiving a lot of attention because, besides its academic interest as a technique for exploring fundamental light-matter interactions [1–4], it has found important practical applications, such as for measuring the concentration of weak constituents of a gaseous mixture [5], for the high-precision atomic clocks [6–8] used in global positioning systems and telecommunications, for frequency stabilization of diode lasers via locking to atomic or molecular absorption lines [9–12], etc.

Semiconductor lasers are ideal devices for many basic research laboratories as well as for different technological applications. The laser spectral characteristics happen to be too poor for several of these uses and special techniques are required to narrow the linewidth and to improve the frequency stability [13]. Increasing the selectivity of the optical cavity through an extended cavity and locking the emission to an atomic or molecular transition are mechanisms to achieve the needed performance [14]. The reliability of lasers with high antireflection coatings opens the way to build lasers with extended cavities, which may be locked to atomic transitions. On the other hand, all-optical stabilization techniques are suitable for laser stabilization, for being intrinsically fast and simple, for allowing compact configurations and for having great robustness. In this sense, intracavity absorbers are one way to optically couple the laser frequency to an atomic line without almost any supplementary electronics [15]. Therefore, studies of semiconductor lasers with intracavity atomic absorbers are important for potential appli-

cations in metrology and high-resolution spectroscopy [16]. In addition, the behavior of such systems may present a variety of interesting dynamical effects in intensity [17] as well as in frequency [18].

The motivation of the present work is to provide a theoretical interpretation of the experimental observations reported in [18], where a cell containing cesium vapor was placed inside a cavity whose gain medium was a semiconductor junction (SJ). The front face of the SJ had an antireflection coating (reflectivity $\leq 5 \times 10^{-4}$), and thus, a reflector was needed to close the cavity and produce laser oscillation. This was achieved via a diffraction grating (DG), and by varying the DG angle (controlled by a piezoelectric device), the lasing frequency could be scanned across the Doppler-broadened D_2 line in the Cs spectrum. Under suitable conditions the lasing frequency was observed to be locked, either to a hyperfine transition (Lamb dip) or to a crossover resonance of the Cs spectrum. A similar earlier experiment was done in [19], the difference being that in [19] a conventional diode laser was employed and the vapor cell was placed in an *external* cavity (resulting in dispersive frequency-selective optical feedback); while in [18], the vapor cell was placed *inside* the laser cavity: the semiconductor junction had antireflection coating and the DG was needed to close the cavity and to produce tunable laser oscillation.

We propose a model based on the usual rate equations for single-mode semiconductor lasers, modified to incorporate phenomenologically the dispersive losses and the dispersive refractive index change caused by the presence of the Cs vapor cell in the laser cavity. We show that the model predictions are in good qualitative agreement with the observations when the emission is single mode, and we discuss the extension of the model to account for multimode emission.

In the experiments of [18] only a small region of the DG was illuminated; thus, the cavity frequency selectivity was poor and either multimode or monomode emission was ob-

*cristina.masoller@upc.edu

†oria@otica.ufpb.br

‡ramon.vilaseca@upc.edu

served, depending on the injection current. The cavity length was about 12 cm long and therefore, when the emission was multimode, the frequency split between the longitudinal modes was about 1.25 GHz, much shorter than that in conventional diode lasers, where it exceeds 100 GHz.

Because of the small frequency separation, the spatial and the dynamic modulation of the carrier density is expected to play a relevant role in the dynamics: the spatial carrier grating (that is due to the counterpropagating waves in the Fabry-Pérot cavity) contributing to nonlinear gain of the longitudinal modes, while the dynamic modulation of the carrier density, resulting in four-wave mixing effects. Therefore, modeling the multimode situation is a challenging task and here we attempt a first step by investigating the predictions of two multimode models that have been used in the literature [20–25], which differ in the way the longitudinal modes are coupled to the carrier density.

One model, referred to as model A, is the conventional model used for multimode diode lasers [26], which neglects the spatial grating in the carrier density. In this model the longitudinal modes are coupled to a single carrier variable representing the spatially averaged carrier density value. The model assumes that carrier diffusion is fast enough to completely wash out the effect of spatial hole burning, i.e., to wash out the spatial grating in the carrier density burned by the standing waves in the Fabry-Pérot cavity.

The second model, referred to as model B, was proposed in Ref. [23] and takes into account the spatial grating in the carrier density by coupling each longitudinal mode to a carrier variable representing the spatially averaged carrier density value and a Fourier harmonic of the spatial grating. Because of the small frequency separation, in both models the longitudinal modes are assumed to have the same gain and losses. As will be shown below, the simulations qualitatively reproduce some of the features observed experimentally in the multimode situation, and suggest that model B in the limit of large cross-coupling parameter β (representing strong carrier diffusion) gives a better agreement with the experiments than model A.

This paper is organized as follows: In Sec. II we present the single-mode model and discuss the various simplifications involved. In Sec. III we present the results of the simulations, characterizing the absorption spectrum in terms of various model parameters. In Sec. IV we investigate the situation in which the laser is locked to a Lamb or crossover dip. We calculate the intensity noise spectrum, the frequency noise spectrum, and the Allan variance [27], which is a measurement of frequency stability in the time domain. In Sec. V we extend the model to consider multimode emission. Section VI presents a summary and the conclusions.

II. MODEL

The rate equations for the linearly polarized slowly varying single-mode intracavity field, E , within the uniform field approximation, and the carrier density in the semiconductor active medium, N , are

$$\frac{dE}{dt} = i\theta E + k(1 + i\alpha)(N - 1)E + C_{at}(i\beta_{at} - \alpha_{at})E + \sqrt{\beta_{sp}}\xi, \quad (1)$$

$$\frac{dN}{dt} = \gamma_N(\mu - N - N|E|^2), \quad (2)$$

where k , α , β_{sp} , γ_N , and μ have the usual meaning: k represents the nonresonant cavity losses (i.e., in the absence of the Cs vapor cell, or when the lasing frequency is far from the cesium line center), α is the linewidth enhancement factor, β_{sp} is the spontaneous-emission noise strength, ξ is a Gaussian white noise, γ_N is the inverse of the carrier lifetime, and μ is the normalized injection current, the nonresonant threshold being at $\mu_{th}=1$.

The parameter θ represents a frequency shift, the nonresonant lasing frequency being equal to $\omega_1 + \theta$, where ω_1 is the reference frequency, chosen equal to the frequency of the transition between the ground state $F=4$ and the excited state $F'=5$ of the Cs D_2 line. In the simulations the lasing frequency can be scanned via a variation in the parameter θ , allowing a comparison with the experiments of [18], where the lasing frequency was scanned via a variation in the diffraction grating angle.

The dispersive losses and the dispersive refractive index change caused by the presence of the Cs vapor cell in the laser cavity are described through a phenomenological modification of the complex susceptibility: α_{at} represents the absorption in the atomic vapor (including saturation effects), β_{at} represents the corresponding refractive index change, and C_{at} represents the density of atoms in the cell and allows varying the strength of the interaction between the optical field and the atomic medium.

A similar simplistic approach was done in [15], where the dispersive loss caused by the Cs vapor cell was modeled by a modification of the susceptibility. However, because the dispersive losses induced by the vapor cell were assumed to depend on the instantaneous lasing frequency, the model was valid only for describing steady states or a time-evolution slow enough, i.e., a dynamics induced by slow time-varying parameters.

To overcome this restriction we consider that the finite response time of the atomic medium can be taken into account by assuming that the medium can respond to time-averaged values of the lasing frequency, $\omega = \text{Im}(\dot{E}/E)$, and intensity, $|E|^2$, which will be denoted as

$$\langle \omega \rangle = \langle \text{Im}(\dot{E}/E) \rangle, \quad (3)$$

$$\langle I \rangle = \langle |E|^2 \rangle. \quad (4)$$

The averaging time is a model parameter. As will be shown in the next section, this approach gives meaningful results (in the sense that they are in qualitative good agreement with the experimental observations) when the inverse of the averaging time is on the order of typical relaxation rates of the Cs atomic dipoles.

In the experimental results of [18], the fact that the semiconductor laser emission was with almost constant intensity, with some fluctuations but with no trace of passive

Q -switching, or spikelike intensity fluctuations or Shilnikov-type dynamics [17], seems to indicate that a more accurate description of the absorbing vapor cell through the

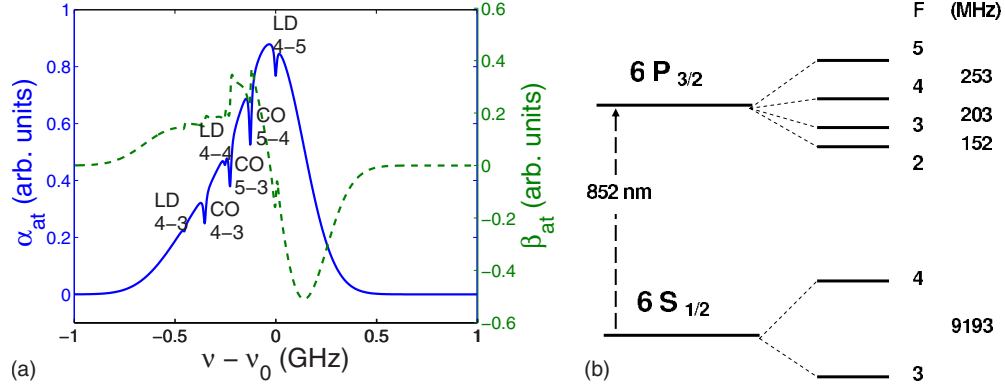


FIG. 1. (Color online) (a) Absorption (solid line) and dispersion (dashed line) coefficients. Three hyperfine Lamb dips (LD) and three crossover resonances (CO) are indicated. (b) Cs D_2 levels.

instantaneous evolution of the atomic level populations and induced electric polarization is not necessary. It might be necessary, perhaps, in cases with larger atomic absorption which could modulate more deeply the emission intensity.

For α_{at} and β_{at} we use phenomenological expressions that are specific to the experimental situation of [18]: an intracavity Cs vapor cell that “sees” two counterpropagating fields. α_{at} and β_{at} take into account three overlapping Doppler-broadened (Gaussian) absorption lines and six narrow dips, corresponding to three Lamb dips and three crossovers. The Doppler lines correspond to transitions from the ground state $F=4$ to the excited states $F'=3, 4$, and 5 of the D_2 line (the Cs D_2 levels are schematically indicated in Fig. 1). The narrow Lamb and crossover dips appear over the broad absorption spectrum when the intracavity forward and backward fields interact resonantly with the same atomic velocity class (atoms with a given component of the velocity along the field propagation axis); the Lamb dips occur when the forward and backward waves are in resonance with the same atomic transition (thus, they appear at the center of each Gaussian Doppler absorption profile), whereas the crossover dips occur when each wave interacts with a different transition.

Taking into account these considerations, α_{at} and β_{at} can be cast as the sum of three Doppler-broadened absorption lines accompanied by their corresponding Lamb dips and three crossover dips which are approximated by inverted Lorentzian line shapes [1,28,29],

$$\alpha_{at} = \left[\sum_{i=1}^3 \alpha_i \frac{\gamma_0(1 + A_i/B_i)}{C_i} \right] \prod_{i \neq j} \left[1 - \frac{c_{co}\gamma_0}{\Omega_{ij}^2 + \gamma^2} \right], \quad (5)$$

$$\beta_{at} = - \sum_{i=1}^3 \alpha_i \Omega_i \left[\frac{2}{\sqrt{\pi}\Delta\omega_g} - \frac{1 - A_i/B_i}{C_i} + \sum_{j \neq i} \frac{c_{co}\Omega_{ij}}{\Omega_{ij}^2 + \gamma^2} \right], \quad (6)$$

where ω_i with $i=1, 2, 3$ are the frequencies of the transitions $F=4 \leftrightarrow F'=5$ ($i=1$), $F=4 \leftrightarrow F'=4$ ($i=2$), and $F=4 \leftrightarrow F'=3$ ($i=3$); $\omega_{ij}=(\omega_i + \omega_j)/2$ are the frequencies of the crossover dips,

$$\Omega_i = \langle \omega \rangle - \omega_i, \quad (7)$$

$$\Omega_{ij} = \langle \omega \rangle - \omega_{ij}, \quad (8)$$

$$\gamma^2 = \gamma_0^2(1 + s\langle I \rangle), \quad (9)$$

$$\alpha_i = c_i \exp(-\Omega_i^2/\Delta\omega_g^2), \quad (10)$$

$$A_i = \sqrt{\Omega_i^2 + \gamma_0^2}, \quad (11)$$

$$B_i = \sqrt{\Omega_i^2 + \gamma^2}, \quad (12)$$

$$C_i = \sqrt{(A_i + B_i)^2 - 4\Omega_i^2}, \quad (13)$$

and $\langle \dots \rangle$ indicates temporal averaging. The coefficient c_i measures the relative weight of the i th transition, while c_{co} measures the depth of the crossover dips. $\Delta\omega_g = (2\pi/\lambda)\sqrt{2 \ln 2} k_B T/m_a$ is the Doppler linewidth and γ_0 is the dip linewidth. The parameter s controls both the saturation of the Doppler absorption line and the depth of the Lamb dip.

The parameters are summarized in Table I. The coefficients c_1 , c_2 , and c_3 were calculated, taking into account the probabilities of the transitions $F=4 \rightarrow F'=5$, $F=4 \rightarrow F'=4$, and $F=4 \rightarrow F'=3$, respectively. Other parameters (the saturation coefficient, s , and the crossover depth, c_{co}) were adjusted phenomenologically such that the absorption profile,

TABLE I. Parameters for α_{at} and β_{at} .

Value	Parameter	Description
1	c_1	Height of Gaussian 1
1/3	c_2	Height of Gaussian 2
7/44	c_3	Height of Gaussian 3
0	ν_1	Center frequency of Gaussian 1
-0.25 GHz	ν_2	Center frequency of Gaussian 2
-0.45 GHz	ν_3	Center frequency of Gaussian 3
0.2 GHz	$\Delta\omega_g/2\pi$	Doppler linewidth
5.22 MHz	$\gamma_0/2\pi$	Dips linewidth
0.5	s	Saturation coefficient
0.02	c_{co}	Crossover depth

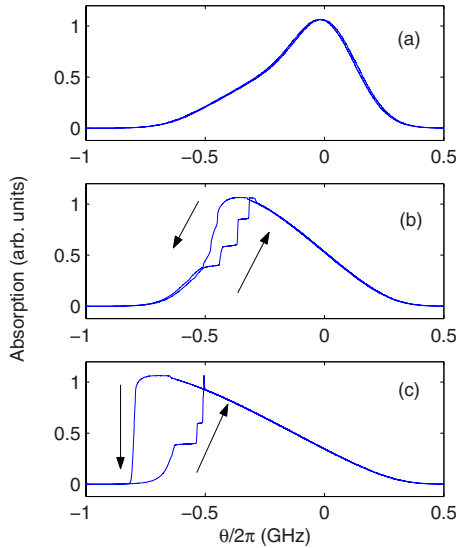


FIG. 2. (Color online) Absorption in the external analysis cell for (a) the laser without the intracavity Cs vapor cell ($C_{at}=0$); with the vapor cell: (b) $C_{at}=0.5$, (c) $C_{at}=1$. The arrows indicate the direction of the hysteresis cycle.

displayed in Fig. 1, agrees qualitatively with the absorption observed experimentally, Fig. 2(a) of [18]. The absorption and dispersion coefficients, α_{at} and β_{at} , are also consistent with those found in [19], which were calculated numerically for Cs atoms using a self-consistent approach of semiconductor laser rate equations together with the density-matrix equation for a multilevel system. To find suitable parameters we took into account the fact that in [19] the Cs vapor cell was placed in the external cavity, while in [18] the Cs vapor cell was inside the cavity and thus larger saturation levels should be expected, resulting in less narrow dips, as compared with [19]. The results of the simulations presented in the next section are, however, rather insensitive to the precise functional forms of α_{at} and β_{at} .

It should be noted that another important simplification of the model is that the optical field is assumed to be uniform inside the whole laser cavity, and time-delay effects are neglected. Delays are well-known sources of instabilities and multistability [15,19], and a more precise modeling of the experimental situation of [18] would involve employing traveling-wave equations for two counterpropagating fields, $E^+(z,t)$ and $E^-(z,t)$, complemented with boundary conditions of the form $E^+(0,t)=r_1E^-(0,t)$ and $E^-(L,t)=r_2E^+(L,t)$, with r_1 and r_2 being the reflectivities of rear laser facet and of the diffraction grating, and L being the extended cavity length.

However, the typical time scales of semiconductor lasers combined with a cavity length of $L=12$ cm as in [18] render this approach impractical, since typical integration steps for semiconductor traveling-wave equations are on the order of $\Delta z=1$ μm and $\Delta t=0.1-0.01$ ps [30]. The model employed here is thus expected to be valid if the extended cavity is not too long (as in [18]), while it should be modified to take into account delays, when modeling situations such as those in [19,31], where the extended cavity is on the order of 0.5 m. Our model can be modified to take into account delays in a

longer cavity by assuming that the Cs vapor responds to the averaged *delayed* values of the lasing frequency and intensity.

To conclude this section we remark that the Cs vapor cell can be seen as an intracavity saturable absorber. The dynamics of lasers with saturable absorbers is a problem with a long history [32,33] and is still the subject of a lot of research not only because it is a well-known technique for mode locking [34], but it also can result in a chaotic output [35]. The standard modeling approach of a laser with a saturable absorber [32,33] assumes that in the laser cavity inversion is not achieved in the whole cavity: in some regions there is amplification of radiation and in others, absorption of radiation (in unpumped regions). The standard equations are Maxwell-Bloch equations with four material variables: the polarization and the population inversion in the absorbing and in the amplifying regions [17]. In our case the amplifying medium is the semiconductor medium, which is characterized by the usual complex susceptibility (the polarization is adiabatically eliminated), while the absorption occurs in the cell filled with cesium vapor. A detailed model of the absorber would thus require the density-matrix formulation (see, e.g., Ref. [19]); however, in the next section it will be shown that the simplistic phenomenological approach of describing the effect of the absorber in terms of frequency- and intensity-dependent absorption and dispersion coefficients proves to be sufficient to describe the main features observed experimentally.

III. RESULTS

We simulated the model equations with typical parameters for the semiconductor active medium, which are, unless otherwise stated, $k=300$ ns⁻¹, $\alpha=5$, $\gamma_N=1$ ns⁻¹, $\mu=2$, and $\beta_{sp}=10^{-5}$ ns⁻¹.

In the experiments of Ref. [18] there were only small variations in the laser intensity; the observed dynamics occurs in the lasing frequency. In order to study this spectral behavior, a small portion of the laser output (of very weak intensity) was analyzed using a second external Cs vapor cell, which was isolated from the laser by an optical isolator to avoid backward reflections. The absorption in this analysis cell was measured under different operating conditions. In the simulations, the absorption in the analysis cell is calculated through an absorption factor with the following spectral profile:

$$\mathcal{F}_{\text{absorption}} = \sum_{i=1}^3 c_i \exp[-(\langle\omega\rangle - \omega_i)^2 / \Delta\omega_g^2]. \quad (14)$$

The analysis cell is outside the cavity and thus it is subject to absorption by only one traveling wave; therefore, no Lamb dips or crossovers appear in Eq. (14). In the simulations the laser intensity is nearly constant [in good agreement with the experiments, see Figs. 3(b) and 3(d) below], and thus the shape of the absorption curve can be used as a frequency discriminator.

As discussed in the previous section, a simplifying assumption of the model is that the response of the intracavity

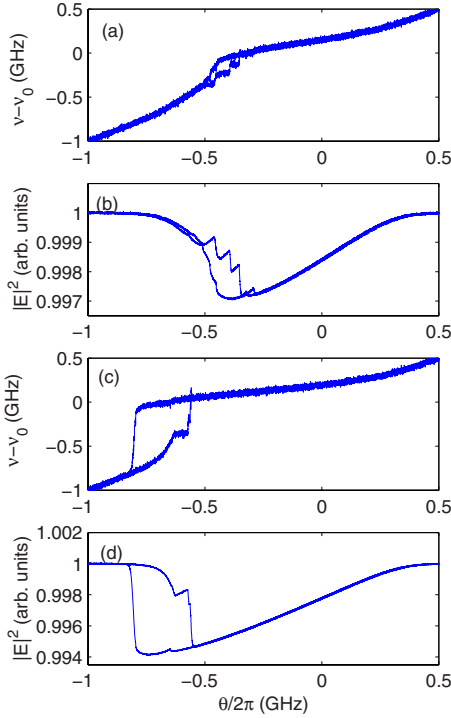


FIG. 3. (Color online) Lasing frequency [(a) and (c)] and intensity [(b) and (d)] vs the detuning θ for [(a) and (b)] $C_{at}=0.5$ and [(c) and (d)] $C_{at}=1$.

Cs vapor cell depends on the time-averaged lasing frequency and intensity. In the following, unless otherwise stated, the averaging time is $\Delta T=10$ ns. This value is chosen because is of the same order of magnitude as the mean atomic dipole lifetime, $T_2 \approx 1/\gamma_0 \approx 30$ ns. The influence of ΔT on the results will be discussed below.

In the experiments of Ref. [18] the lasing frequency was scanned across the D_2 line in the Cs spectrum by varying the angle of the diffraction grating; in the simulations, we scan the lasing frequency by varying θ in Eq. (1). We remark that θ represents the detuning between the “solitary” free-running lasing frequency and the Cs D_2 line center frequency. The parameter θ was scanned using a linear ramp, from $\theta/2\pi=-1$ GHz to $+1$ GHz and back in a time interval equal to $10 \mu\text{s}$.

Figure 2 displays the absorption in the external analysis cell vs θ in the absence [Fig. 2(a)] and in the presence [Figs. 2(a) and 2(b)] of the intracavity Cs vapor cell. Two values are considered for the coefficient C_{at} that measures the strength of the coupling of the light and the Cs atoms: weak coupling [Fig. 2(b)] and stronger coupling [Fig. 2(c)]. It can be observed that there are regions where the absorption is nearly constant, indicating that the lasing frequency is also approximately constant and not controlled by θ . A hysteresis cycle occurs for increasing and decreasing θ , whose size increases with the coupling strength, C_{at} . These results are in good qualitative agreement with the experimental observations, see Fig. 3(b) of [18].

The lasing frequency (measured with respect to the reference frequency which is the center frequency of the D_2 line in the Cs spectrum, i.e., $\omega_1/2\pi$) and the lasing intensity vs θ

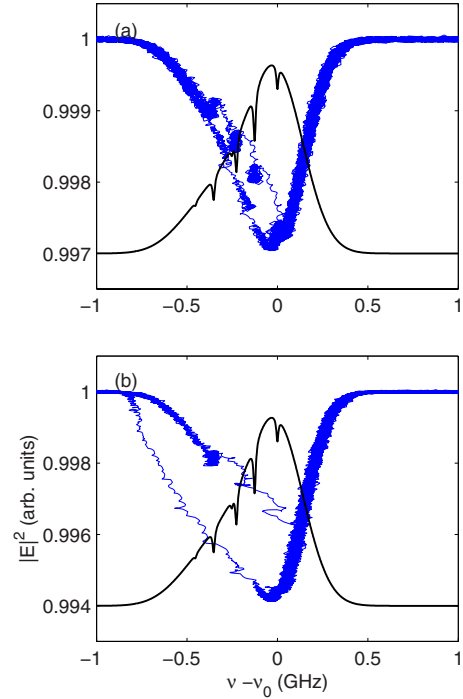


FIG. 4. (Color online) Intensity vs lasing frequency for (a) $C_{at}=0.5$ and (b) 1.0 . For easy comparison the thin line displays a reference absorption curve.

are presented in Fig. 3, for weak and for stronger coupling with the atomic vapor. In order to display more clearly the hysteresis cycle and the locking regions, the intensity noise was partially washed out by averaging it over a time window of 1 ns. It can be observed that there are regions where the frequency is “locked,” i.e., almost constant. The variation in the laser intensity is very small, also in good agreement with the experiments.

In the regions where the frequency is clamped, it is locked to one of the narrow absorption lines of the spectrum of the intracavity Cs vapor. This is shown in Fig. 4, which presents the intensity vs the lasing frequency and, for comparison, the intracavity absorption curve, Eq. (5). The inverted dips which appear in Figs. 4(a) and 4(b) show that the regions of locking occur when the lasing frequency is close to one of the Lamb or crossover dips.

The influence of the depth of the Lamb and crossover dips is analyzed in Fig. 5, where it is seen that pronounced dips (i.e., smaller γ_0) results in larger regions of locking. The interplay of the saturation parameter s and the coupling strength C_{at} is analyzed in Fig. 6, where it is seen that the shape of the absorption curve is in fact determined by the relation between these two parameters: the shape of the curve for large s and large C_{at} , Fig. 6(a), is similar to that for smaller s and smaller C_{at} , Fig. 6(b), the difference between the two cases mainly being in the “locking” regions, which are smaller for larger saturation because the dips become less pronounced.

Other parameters that are of interest are the linewidth enhancement factor, α , which determines the strength of the phase-amplitude coupling in the semiconductor active medium, and the injection current parameter, μ , which deter-

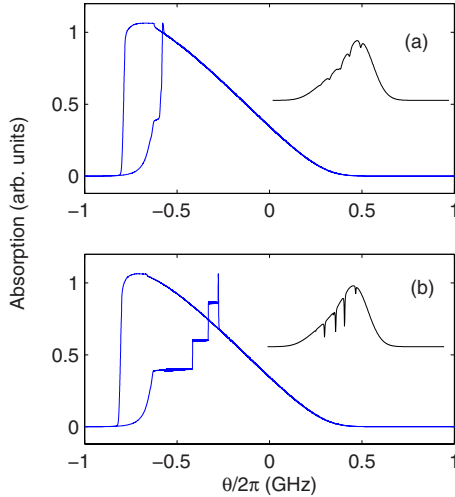


FIG. 5. (Color online) Influence of the dips linewidth: (a) $\gamma_0/2\pi=10.44$ MHz, (b) 2.61 MHz. Other parameters as in Fig. 2(c).

mines the intensity of the laser beam. Their influence is presented in Figs. 7 and 8, where it can be seen that they both modify the size of the hysteresis cycle and shift the absorption curve along the frequency axis.

We conclude this section with a comment on the influence of the response time of the atomic medium, represented by the averaging time ΔT used for computing the frequency and the intensity “seen” by the Cs vapor. Figure 9 displays the absorption curve, for fixed C_{at} and different values of ΔT . When the Cs vapor is assumed to respond instantaneously to variations in the lasing frequency and intensity, instabilities in the absorption curve are seen, Fig. 9(a). This agrees with the well-known fact that a fast response of the absorber is a source of instability [17]. Instabilities are seen for a wide range of response times, $\Delta T=1$ ps to 1 ns [Figs. 9(b)–9(e)]. However, if the response of the Cs vapor is slow enough [$\Delta T=10$ ns, Fig. 9(f)], the instability disappears. We remark

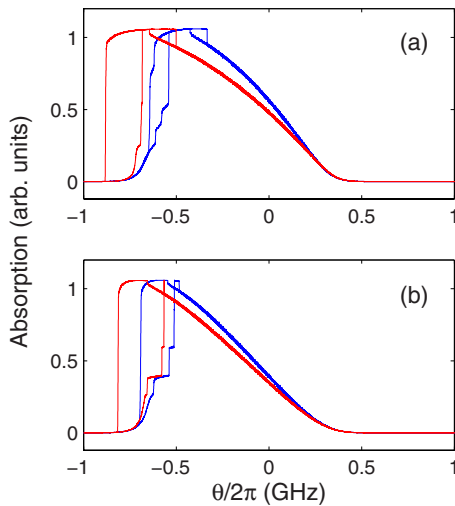


FIG. 6. (Color online) Influence of the saturation parameter: (a) $s=10$ and $C_{at}=2$ (blue), 3 (red); (b) $s=1.0$ $C_{at}=1$ (blue), 1.2 (red). Other parameters as in Fig. 2(c).

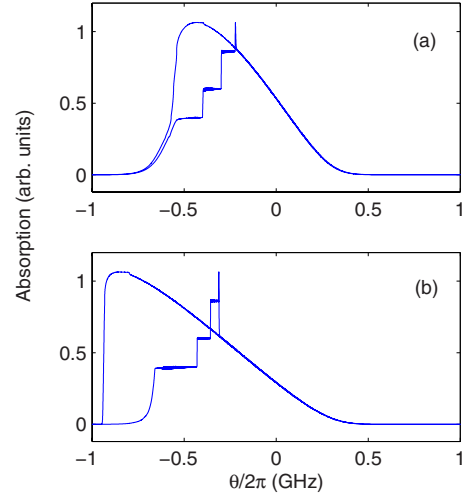


FIG. 7. (Color online) Influence of the linewidth enhancement factor: (a) $\alpha=3$, (b) 6. Other parameters as in Fig. 2(c).

that this slow response time is, as pointed out before, of the same order of magnitude as the mean atomic dipole lifetime, $T_2 \approx 1/\gamma_0 \approx 30$ ns, and is in these more realistic conditions that there is more similarity with the experimental results. Notice also how the influence of the dips disappears when the atomic medium response is fast; we interpret this as due to the fact that the instantaneous lasing frequency presents fast fluctuations. Also, the hysteresis cycle tends to disappear when the response is fast.

IV. ANALYSIS OF THE LOCKING REGIONS

When the lasing frequency is locked to a Lamb or cross-over dip, a reduced laser linewidth and improved frequency stability are expected [15]. The optical spectrum, which is displayed in Fig. 10, presents relaxation-oscillation side peaks that are strongly damped (solid lines), in comparison

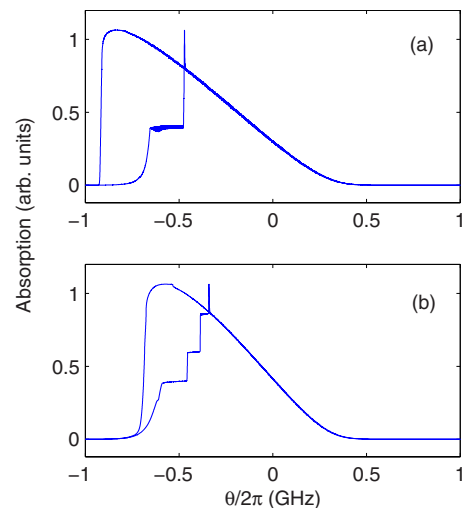


FIG. 8. (Color online) Influence of the injection current parameter: (a) $\mu=1.2$, (b) 3.5. Other parameters as in Fig. 2(c).

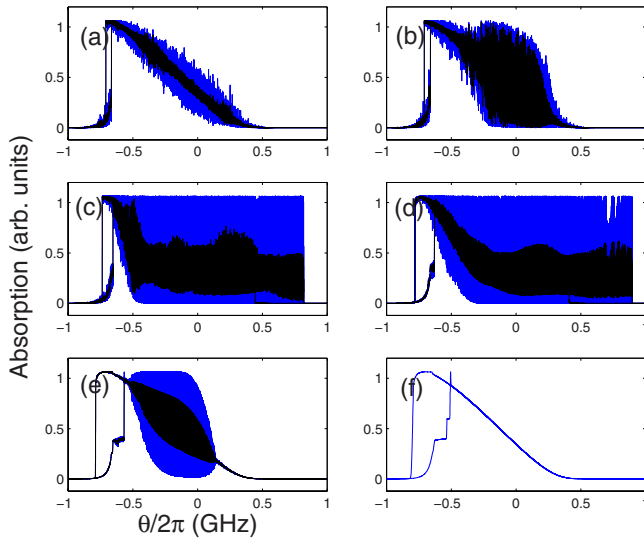


FIG. 9. (Color online) Influence of the averaging time for computing the frequency and the intensity "seen" by the Cs vapor: (a) $\Delta T=0$ ns; (b) 0.001 ns; (c) 0.01 ns; (d) 0.1 ns; (e) 1 ns; (f) 10 ns. The black line is the absorption when is averaged over 1 ns to simulate the finite bandwidth of the detectors. Other parameters as in Fig. 2(c).

with those when the laser is not resonant with the Cs vapor (dashed lines). This effect is more pronounced with increasing the coupling strength, C_{at} .

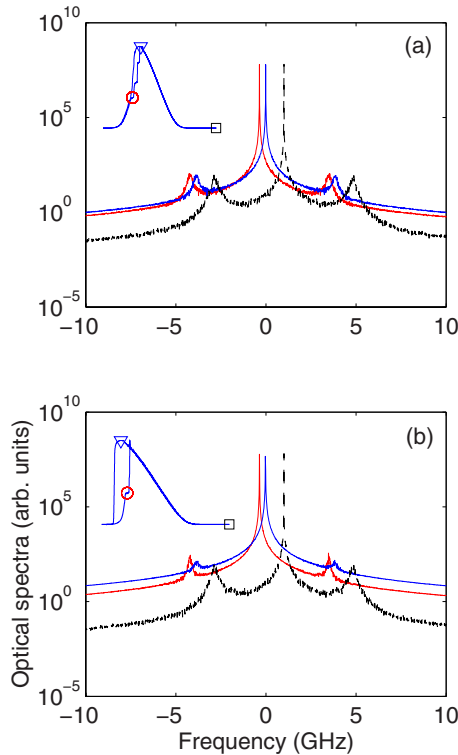


FIG. 10. (Color online) Optical spectrum when the laser frequency is locked to a dip of the intracavity absorber (solid lines), and when is not resonant with the absorber (dashed line). (a) $C_{at}=0.5$, (b) 1.0. The insets show the points where these spectra are calculated.

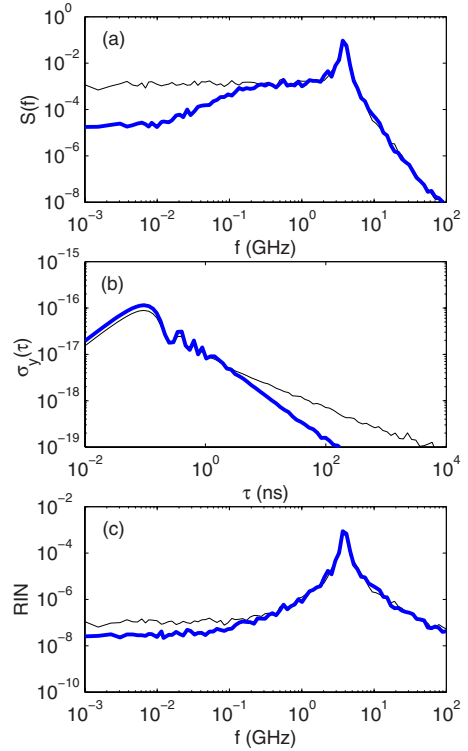


FIG. 11. (Color online) (a) Frequency noise spectrum; (b) Allan deviation [square root of Allan variance, Eq. (15)]; (c) Intensity noise spectrum. The thick line is when the lasing frequency is locked to a dip [parameters are as in Fig. 10(b)]; the thin line is for the free-running laser.

Figure 11(a) displays the spectral density of the frequency fluctuations (the thick line is for the laser locked to a dip, while the thin line is for the free-running laser). The frequency range corresponds to short-term fluctuations (frequencies above 1 MHz). Reduction in the frequency noise in this region is usually associated with reduction in laser linewidth. Because of the time scales of the model we cannot compute the low-frequency part of the noise spectrum (<1 MHz), which is responsible for slow drift of the laser line, and is associated with frequency instability. Even if the model allowed for long time simulations, the results will be of limited application because for a realistic estimation of long-term stability, the influence of slow thermal effects and mechanical instabilities should be taken into account in the model.

Short-term frequency fluctuations can be quantified in the time domain by the Allan variance [15], $\sigma_y^2(\tau)$,

$$\sigma_y^2(\tau) = \frac{1}{2} \langle (y_{n+1} - y_n)^2 \rangle, \quad (15)$$

where y_n is the normalized frequency error, averaged over sample period n , $y_n = \langle \delta\nu / \nu \rangle$, and τ is the sampling interval. The result is shown in Fig. 11(b), in which the variance calculated for the free-running laser is also shown (thin line). It can be confirmed that the short-term stability of the laser is improved by the presence of the Cs vapor cell. In addition, the intensity noise is also reduced, as shown in Fig. 11(c).

V. MULTI-LONGITUDINAL-MODE OPERATION

While the model presented in the previous section explains qualitatively well several features observed in [18] (such as the hysteresis cycle and the locking regions), other features (such as the “periodic” instabilities in Fig. 4 of [18]) have not been seen in the simulations.

In the experiments the cavity frequency selectivity of the DG was poor so that monomode or multimode emission was observed, depending on the semiconductor junction current. When the laser was multimode, in the regions of locking the laser became monomode. Since the cavity length was about 12 cm long, the frequency split between the longitudinal modes, $\Delta\nu=c/(2L)$, was about 1.25 GHz, much shorter than in conventional edge emitters, where the mode split exceeds 100 GHz.

Because of the small frequency separation, modeling the multimode situation is a challenging task. Here we employ two models for multimode diode lasers that have been proposed in the literature [20–26]. Both models perform a modal expansion of the optical field but differ in the coupling of the longitudinal modes with the carrier density. One model, which following Ref. [25] we refer to as model A, assumes that carrier diffusion is fast and therefore the spatial grating in the carrier density (burned by the counterpropagating waves in the Fabry-Pérot cavity) can be neglected. This model couples the modal field amplitudes, E_m , to a single carrier density, N , representing the spatially averaged carrier density.

The second model, which following Ref. [25] we refer to as model B, takes into account the spatial grating by performing an expansion of the carrier density in spatial harmonics. In this model the modal field amplitudes, E_m , are coupled to nonlinear modal gains, N_m , that include both the average value of the carrier density and the spatial harmonic representing the grating.

The rate equation for the complex field modal amplitudes is the same for both models,

$$\begin{aligned} \frac{dE_m}{dt} = & i\theta E_m + k(1+i\alpha)(N_m-1)E_m \\ & + C_{at}(i\beta_{at,m} - \alpha_{at,m})E_m + \sqrt{\beta_{sp}}\xi. \end{aligned} \quad (16)$$

In model A, the rate equation for the carrier density is

$$\frac{dN}{dt} = \gamma_N \left(\mu - N - N \sum_m^M |E_m|^2 \right). \quad (17)$$

In model B, there are M rate equations for the modal gains

$$\frac{dN_m}{dt} = \gamma_N \left(\mu - N_m - N_m \sum_n^M \beta_{mn} |E_n|^2 \right), \quad (18)$$

where M is the number of longitudinal modes.

Because the gain spectrum of semiconductor media is rather flat, and because we are considering a situation in which the frequency separation between the modes is small, all the modes are assumed to have the same gain and losses. The phenomenological cross-saturation parameters $0 \leq \beta_{mn} \leq 1$ in Eq. (18) measure the mode-mode coupling due to

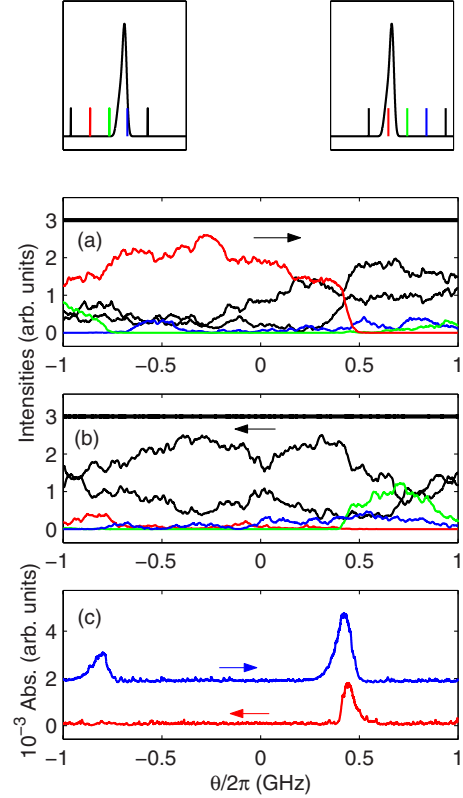


FIG. 12. (Color online) Results of simulations of model A with $M=5$, $\mu=4$, and $C_{at}=1$. Evolution of the modal intensities as the detuning θ is scanned (a) up and (b) down across the absorber line. We show the initial and final position of the modes relative to the absorption line (top, left, and right, respectively). The arrows indicate the direction of the scan. (c) Absorption, calculated using Eq. (20), during the up scan (top line, shifted vertically for clarity) and the down scan (bottom line).

carrier density gratings [25]. They are also assumed to be mode independent: $\beta_{mn}=\beta$ for $m \neq n$, and $\beta_{mm}=1$. With this assumption Eq. (18) can then be rewritten as

$$\frac{dN_m}{dt} = \gamma_N \left[\mu - N_m - N_m \beta \left(\sum_n^M |E_n|^2 \right) - N_m (1 - \beta) |E_m|^2 \right], \quad (19)$$

where one can notice that model B is equal to model A if $\beta=1$ ($N_m=N \forall m$), and is equal to the single-mode model studied in the previous section if $\beta=0$ (in this case each mode is coupled to its own carrier density and they are uncoupled one of another).

In the rate equation for the optical field of the m th mode, Eq. (16), the absorption and the dispersion induced by the Cs vapor cell, $\alpha_{at,m}$ and $\beta_{at,m}$, are calculated as in the single-mode situation, now taking into account the time-averaged intensity and frequency of the m th longitudinal mode, $\langle I_m \rangle$ and $\langle \omega_m \rangle$, respectively [with the instantaneous values being $I_m=|E_m|^2$ and $\omega_m=\text{Im}(\dot{E}_m/E_m)$]. Other parameters in Eqs. (16)–(18) have the same meaning as in the previous section.

Figure 12 presents results of simulations of model A, with $M=5$. The modal intensities are shown vs the detuning θ ,

which is scanned linearly, from $\theta/2\pi = -1$ GHz to 1 GHz, in Fig. 11(a) and back, from $\theta/2\pi = 1$ GHz to -1 GHz, in Fig. 11(b). The insets display the position of the longitudinal modes relative to the absorption line: for $\theta/2\pi = -1$, left; for $\theta/2\pi = 1$, right. It can be seen that at the beginning of the upward scan, Fig. 12(a), the mode that is resonant with the absorber (blue online) is off, as a consequence of having larger cavity losses than the other modes (due to absorption by the intracavity vapor cell). As θ increases this mode becomes not resonant, its cavity losses become smaller, and its intensity builds up. The consecutive mode on the left frequency side (green online) now becomes resonant with absorber and experiences stronger losses. As a result, its intensity decreases to the noise level. As the scan continues this mode turns on again when it becomes not resonant with the absorber, and the consecutive mode on the left frequency side (red online) becomes resonant, has larger losses, and rapidly drops off. The inverse sequence is observed during the reverse scan, Fig. 12(b): going from $\theta/2\pi = 1$ GHz to -1 GHz the red mode turns off, then the blue one, and then the green one. During the scans the total intensity, $\sum_m |E_m|^2$, is not affected by the mode switching sequence and remains nearly constant in time ($\cong \mu - 1$).

The absorption in the external analysis cell, calculated as the sum of the absorption experimented by each longitudinal mode [using Eq. (14)],

$$\begin{aligned}
 \mathcal{F}_{\text{absorption}} &= \sum_{m=1}^M \mathcal{F}_{\text{absorption}}(i) \\
 &= \sum_{m=1}^M \left(\sum_{i=1}^3 c_i \exp[-(\langle \omega_m \rangle - \omega_i)^2 / \Delta \omega_g^2] \right) \langle I_m \rangle,
 \end{aligned} \tag{20}$$

is displayed in Fig. 12(c). Notice that the contribution of the m th longitudinal mode to the absorption depends on both its time-averaged frequency, $\langle \omega_m \rangle$, and intensity, $\langle I_m \rangle$. The dependence of the absorption with the intensity in the single-mode situation, Eq. (14), was neglected because the intensity is nearly constant, as shown in Figs. 3(b) and 3(d).

The longitudinal modes whose frequencies are far from the absorption line do not contribute to the absorption because the exponentials in Eq. (20) are almost zero. The longitudinal mode that is resonant with the absorber has intensity at the noise level (is off because of increased losses) also does not contribute to the sum in the absorption expression, Eq. (20), because $\langle I_m \rangle \approx 0$. In consequence, the longitudinal modes that contribute to the absorption are the two neighbors of the resonant one. We note also that, in the context of this model, no spectral hole burning effect is expected in the absorber profile because the longitudinal mode that is resonant with the absorber does not develop significant intensity, i.e., no Lamb dips or crossover dips appear in the absorber profile.

For a larger value of C_{at} , representing a denser vapor, Fig. 13, the intensities of the longitudinal mode resonant with the absorber and also, of the two neighboring modes, drop to the noise level, and thus the vapor becomes transparent (the absorption being almost a flat line) because the surviving

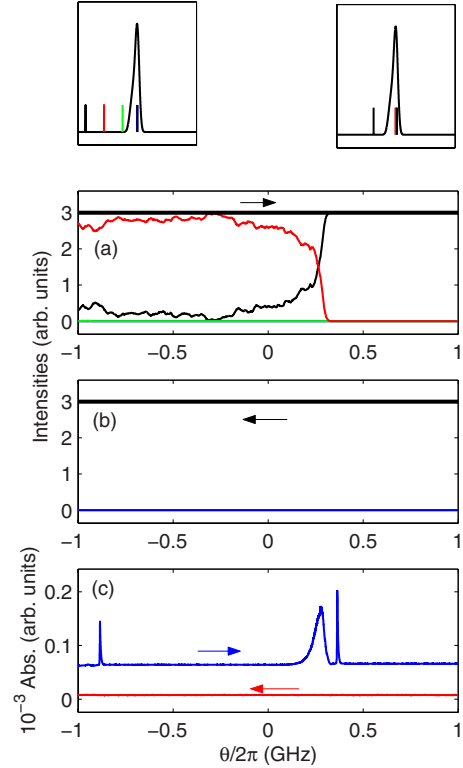


FIG. 13. (Color online) Results of simulations of model A with $M=5$, $\mu=4$, and $C_{at}=50$.

modes are those that are farthest from the absorption line [and for these modes, the exponentials in Eq. (20) are negligible].

Let us now describe results of simulations of model B, shown in Figs. 14 and 15, for two values of the cross-saturation coefficient β . When β is not too large, Fig. 14, the longitudinal mode that is resonant with the absorber decreases slightly its intensity (because of increased losses due to the intracavity absorber) but it does not turn off because of nonlinear gain representing the carrier grating. The absorption curve of the analysis cell, Fig. 14(c), is similar to that found in the single-mode situation; however, because the modes do not turn off when they are in resonance with the intracavity absorber, the absorption in the analysis cell is the superposition of the absorption of each mode. In the limit of β very close to unity, Fig. 15, the dynamics approaches that predicted by model A, but the mode switching on and off is more abrupt. This results in an absorption curve that has more features, resembling more the experimental observations.

The fact that in the simulations we have not seen the periodic instabilities observed in Fig. 4 of [18] can be perhaps attributed to four-wave mixing (FWM) effects due to the dynamic modulation of the carrier density at the longitudinal-mode frequency split. Since the carrier density cannot be modulated at frequencies much higher than γ_N , FWM is negligible in conventional edge emitters, but it can have a large impact in our situation because the frequency split is comparable to γ_N . The investigation of FWM effects, using more sophisticated multimode models such as those proposed in Refs. [36,37], is outside the scope of the present work and is left for future work.

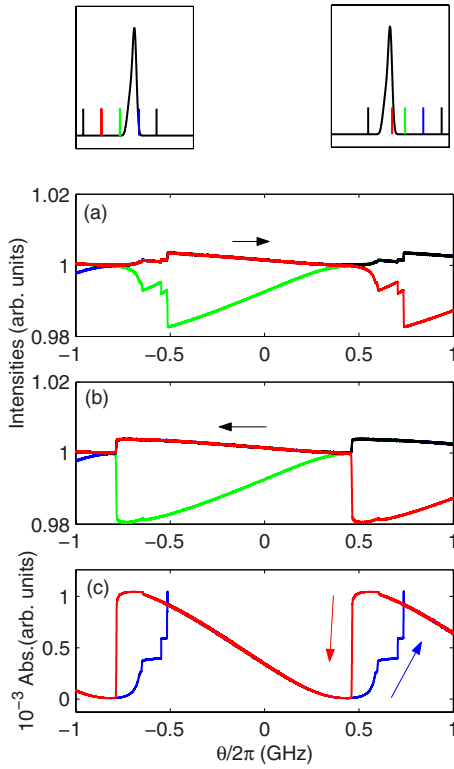


FIG. 14. (Color online) Results of simulations of model B with $M=5$, $\beta=0.5$, $\mu=4$, and $C_{at}=1$.

VI. CONCLUSION

We studied the dynamics of a semiconductor laser with an intracavity atomic absorber. Our study was motivated by the experiments of Barbosa *et al.* [18], where a cesium vapor cell was placed inside the cavity formed by a semiconductor junction, whose output face was antireflection coated, and a diffraction grating (DG) was needed to close the cavity and produce tunable laser oscillation. We proposed a model for a single-mode laser that takes into account phenomenologically the frequency-dependent absorption and dispersion due to the intracavity vapor cell. Simulations of the model equations clearly showed the crucial roles of the Lamb dips and crossover resonances, as well as the absorber response time. Qualitative agreement with the experimental results of [18] in several basic features has been found. This, together with the fact that in the experimental results the semiconductor laser emitted with almost constant intensity, with some fluctuations but with no trace of passive Q -switching, or deterministic spikelike intensity fluctuations or Shilnikov-type dynamics [17], seem to confirm our assumption (pointed out in Sec. II) that a more accurate description of the absorbing vapor cell through the instantaneous evolution of the atomic level populations and induced electric polarization is not required. Such more accurate description might be necessary, perhaps, in cases with larger atomic absorption (brought about for instance by a larger atomic density), which could modulate more deeply the emission intensity. It can also be pointed out here that the fluctuations in frequency and intensity that the spontaneous emission in the semiconductor medium introduces (in smaller or larger degree depending on

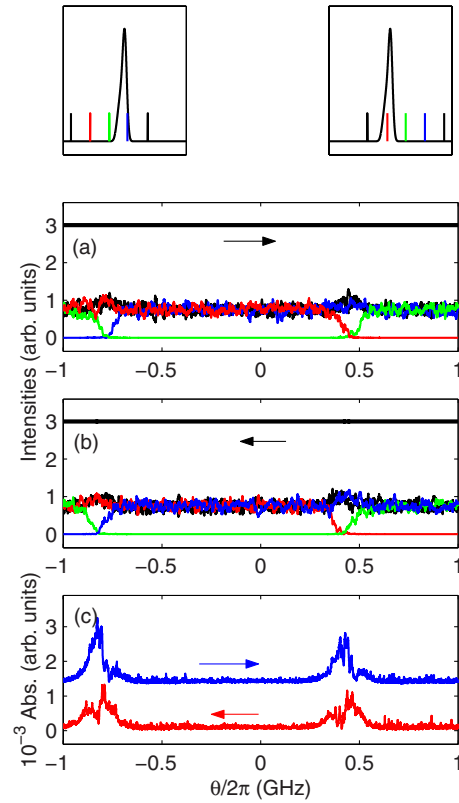


FIG. 15. (Color online) Results of simulations of Model B with $M=5$, $\beta=0.9999$, $\mu=4$, and $C_{at}=1$.

the operating conditions) in the laser emission probably also contribute, to some degree, to avoiding deterministic long evolutions of the atomic population in the vapor cell, since field phase fluctuations inhibit transfer of coherence effects to the atoms.

On the other hand, the comparison with the experimental results of [18] has allowed us to estimate in some measure the range of values, for several of the parameters, for which the observed behaviors can exist. In particular, and still within the single-mode approach, we have discussed in which conditions the Lamb dip and crossover resonances can manifest as frequency lockings in the laser emission. Too small saturations ($s \ll 1$), which make the Lamb dips shrink, or too large saturations ($s \gg 10$), which make them broaden, wash out the frequency-locking features in the laser emission. The effect of a large saturation, however, can be partially compensated by increasing the atomic density, with the limit that too large atomic densities could make laser emission intensity to disappear or, perhaps, to become strongly time dependent (conditions which are out of the scope of the present work). The saturation values considered here for the interaction of the laser light with the atoms in the vapor cell can fit reasonably well those of the experiments in Ref. [18] if it is taken into account that the effective saturation in the experiments was reduced in many cases by the spontaneous-emission-induced frequency fluctuations and, when applicable, by the multimode character of the laser light.

We extended the study to take into account multimode emission. We investigated the predictions of two models that differ in the way the longitudinal modes are coupled to the

carrier density. One model, referred to as model A, neglects the spatial grating in the carrier density burned by the counterpropagating waves in the Fabry-Pérot cavity. In this model the longitudinal modes are coupled to a single carrier variable representing the spatially averaged carrier density. The second model, referred to as model B, takes into account the spatial grating by coupling each mode to a carrier variable representing the spatially averaged carrier value and a Fourier harmonic of the spatial grating. Simulations of model A suggest that the longitudinal mode that is resonant with the intracavity atomic vapor turns off because it experiences larger losses than the other modes; the laser emits in the other modes that do not experience significant distortion (absorption and dispersion) due to the intracavity absorber. The predictions of model B depend on the parameter β that controls the strength of mode-mode coupling. When β is not too large, the mode resonant with the intracavity absorber does not turn off (but its intensity diminishes because of the absorber, while the intensities of the other modes grow), and the absorption in the external analysis cell resembles that of the single-mode situation, but is a superposition of the absorption due to coexisting modes. In the limit of β very close to unity, corresponding to very fast carrier diffusion, the dynamics resembles that predicted by model A, but the mode switching is more abrupt and more features appear in the

absorption curve of the analysis cell, giving a better agreement with the experiments. However, the periodic instabilities observed experimentally in Fig. 4 of [18] were not found in simulations of neither model. While we cannot rule out the existence of parameters that will fit the observations (the dynamics of model B depends strongly on the parameter β ; the duration of the scan and the coupling strength with the intracavity absorber are key parameters in both models), we expect that the models will give a better agreement with the experiments if four-wave mixing effects are taken into account. They should play an important role because of the small value of the mode frequency split (which is of the order of the carrier decay rate). The extension of these models to include four-wave mixing effects is outside of the scope of the present work and is left for future work.

ACKNOWLEDGMENTS

C.M. acknowledges support from the “Ramon y Cajal” Program, the Spanish Ministerio de Educacion y Ciencia through Grant No. FIS2005-07931-C03-03, and the U.S. Air Force Office of Scientific Research through Grant No. FA9550-07-1-0238. R.V. and C.M. also acknowledge support from the Generalitat de Catalunya through Project No. 2005SGR00457.

-
- [1] W. Demtröder, *Laser Spectroscopy: Basic Concepts and Instrumentation*, 3rd ed. (Springer-Verlag, Berlin, 2003).
- [2] R. S. Bennink, V. Wong, A. M. Marino, D. L. Aronstein, R. W. Boyd, C. R. Stroud, Jr., S. Lukishova, and D. J. Gauthier, *Phys. Rev. Lett.* **88**, 113901 (2002).
- [3] V. Wong, R. W. Boyd, C. R. Stroud, Jr., R. S. Bennink, and A. M. Marino, *Phys. Rev. A* **68**, 012502 (2003).
- [4] L. S. Cruz, D. Felinto, J. G. A. Gomez, M. Martinelli, P. Valente, A. Lezama, and P. Nussenzveig, *Eur. Phys. J. D* **41**, 531 (2007).
- [5] P. Werle, F. Slemr, K. Maurer, R. Kormann, R. Mucke, and B. Janker, *Opt. Lasers Eng.* **37**, 101 (2002).
- [6] R. Wynands and S. Weyers, *Metrologia* **42**, S64 (2005).
- [7] W. H. Oskay, S. A. Diddams, E. A. Donley *et al.*, *Phys. Rev. Lett.* **97**, 020801 (2006).
- [8] J. Camparo, *Phys. Today* **60**(11), 33 (2007).
- [9] C. J. Cuneo, J. J. Maki, and D. H. McIntyre, *Appl. Phys. Lett.* **64**, 2625 (1994).
- [10] R. N. Li, S. T. Jia, D. Bloch, and M. Ducloy, *Opt. Commun.* **146**, 186 (1998).
- [11] A. F. A. da Rocha, P. C. S. Segundo, M. Chevrollier, and M. Oria, *Appl. Phys. Lett.* **84**, 179 (2004).
- [12] E. A. Gazazyan, A. V. Papoyan, D. Sarkisyan, and A. Weis, *Laser Phys. Lett.* **4**, 801 (2007).
- [13] C. E. Wieman and L. Hollberg, *Rev. Sci. Instrum.* **62**, 1 (1991).
- [14] L. Ricci, M. Weidemüller, T. Esslinger, A. Hemmerich, C. Zimmermann, V. Vuletic, W. König, and T. W. Hänsch, *Opt. Commun.* **117**, 541 (1995).
- [15] J. M. Iannelli, Y. Shevy, J. Kitching, and A. Yariv, *IEEE J. Quantum Electron.* **29**, 1253 (1993).
- [16] S. Knappe, H. G. Robinson, and L. Hollberg, *Opt. Express* **15**, 6293 (2007).
- [17] C. O. Weiss and R. Vilaseca, *Dynamics of Lasers* (VCH Publishers, New York, 1991).
- [18] L. B. Barbosa, T. Sorrentino, D. N. Ferreira, D. Reyes Ardila, M. Chevrollier, and M. Oria, *Opt. Lett.* **32**, 1869 (2007).
- [19] F. Di Teodoro, E. Cerboneschi, D. Hennequin, and E. Arimondo, *Quantum Semiclass. Opt.* **9**, 867 (1997).
- [20] F. Rogister, P. Megret, O. Deparis, and M. Blondel, *Phys. Rev. A* **62**, 061803(R) (2000).
- [21] D. W. Sukow, T. Heil, I. Fischer, A. Gavrielides, A. Hohl-AbiChedid, and W. Elsasser, *Phys. Rev. A* **60**, 667 (1999).
- [22] J. M. Buldú *et al.*, *J. Opt. B: Quantum Semiclassical Opt.* **4**, 415 (2002).
- [23] E. A. Viktorov and P. Mandel, *Phys. Rev. Lett.* **85**, 3157 (2000).
- [24] P. Mandel, E. A. Viktorov, C. Masoller, and M. S. Torre, *Physica A* **327**, 129 (2003).
- [25] I. V. Koryukin and P. Mandel, *Phys. Rev. A* **70**, 053819 (2004).
- [26] G. P. Agrawal, *Long Wavelength Semiconductor Lasers* (Van Nostrand Reinhold, New York, 1986).
- [27] D. W. Allan, *Proc. IEEE* **54**, 211 (1966).
- [28] S. Stenholm, *Foundations of Laser Spectroscopy* (Wiley, New York, 1984).
- [29] S. Mandal and P. N. Ghosh, *Phys. Rev. A* **45**, 4990 (1992).
- [30] C. Serrat and C. Masoller, *Phys. Rev. A* **73**, 043812 (2006).
- [31] J. Kitching, A. Yariv, and Y. Shevy, *Phys. Rev. Lett.* **74**, 3372 (1995).

- [32] M. Tachikawa, F.-L. Hong, K. Tani, and T. Shimizu, Phys. Rev. Lett. **60**, 2266 (1988).
- [33] B. Zambon, Phys. Rev. A **44**, 688 (1991).
- [34] M. Yoshita, M. Kuramoto, M. Ikeda, and H. Yokoyama, Appl. Phys. Lett. **94**, 061104 (2009).
- [35] H. L. D. de S. Cavalcante and J. R. Rios Leite, Chaos **18**, 023107 (2008).
- [36] M. Ahmed and M. Yamada, IEEE J. Quantum Electron. **38**, 682 (2002).
- [37] A. M. Yacomotti, L. Furfaro, X. Hachair, F. Pedaci, M. Giudici, J. Tredicce, J. Javaloyes, S. Balle, E. A. Viktorov, and P. Mandel, Phys. Rev. A **69**, 053816 (2004).